

# REPORT DOCUMENTATION PAGE

AFRL-SR-BL-TR-01-

Please estimate the burden for this collection of information is estimated to average 1 hour per response, including the gathering and maintaining the data needed, and completing and reviewing the collection of information. Send comments regarding this burden estimate or any other aspect of this collection of information, including suggestions for reducing the burden, to Washington Headquarters Services, Directorate for Information Operations and Reports, 1215 Jefferson Davis Highway, Suite 1204, Arlington, VA 22202-4302, and to the Office of Management and Budget, Paperwork Reduction Project (0308-0188), Washington, DC 20503.

0308

1. AGENCY USE ONLY (Leave blank)		2. REPORT DATE 3/2/01		3. REPORT TYPE AND DATES COVERED Final Technical 6/1/97-5/31/00	
4. TITLE AND SUBTITLE Interleaving and Apodization for Volume Optical Storage				5. FUNDING NUMBERS F49620-97-1-0469	
6. AUTHOR(S) Dr. Mark A. Neifeld					
7. PERFORMING ORGANIZATION NAME(S) AND ADDRESS(ES) The Department of Electrical & Computer Engineering The College of Engineering and Mines The University of Arizona Tucson, AZ 85721				8. PERFORMING ORGANIZATION REPORT NUMBER	
9. SPONSORING / MONITORING AGENCY NAME(S) AND ADDRESS(ES) AFOSR/NE 801 N Randolph St Rm 732 Arlington, VA 22203-1977				10. SPONSORING / MONITORING AGENCY REPORT NUMBER	
11. SUPPLEMENTARY NOTES					
12a. DISTRIBUTION / AVAILABILITY STATEMENT Approved for Public Release - Distribution is Unlimited				12b. DISTRIBUTION CODE	
13. ABSTRACT (Maximum 200 words)  [2] ABSTRACT: Optical storage systems offer the potential for drastically increased data transfer rates through the use of parallel access. The fidelity and capacity of these optical systems are impacted by the interfaces used to access the parallel data. In particular, the coding and signal processing components of the system must be designed with the 2D data format in mind. This research has focused on novel methods of coding both the object arms (e.g., interleaving) and the reference arms (e.g., apodizing) of holographic optical storage systems. Our research efforts have produced several significant results: (1) An information-theoretic methodology has been established for quantifying the performance of VH systems, (2) A multidimensional interleaving strategy has been developed for optimizing bit positions within a 2D channel, (3) An information-based design paradigm has been implemented for the design of data-bearing optical systems, and (4) Tradeoffs concerning the balance of noise reduction with storage density have been produced for both apodized and unapodized systems. Item (4) concerns work that is not yet published and a copy of an internal report describing this work is attached.					
14. SUBJECT TERMS				15. NUMBER OF PAGES	
				16. PRICE CODE	
17. SECURITY CLASSIFICATION OF REPORT UNCLASSIFIED		18. SECURITY CLASSIFICATION OF THIS PAGE UNCLASSIFIED		19. SECURITY CLASSIFICATION OF ABSTRACT UNCLASSIFIED	
				20. LIMITATION OF ABSTRACT UNLIMITED	

20010508 063

**AFOSR FINAL REPORT 8/31/00**

[1] COVER SHEET:

Title:

Interleaving and Apodization for Volume Optical Storage

Grant Number:

F49620-97-1-0469

PI name:

Dr. Mark A. Neifeld

Institution:

University of Arizona

Department of Electrical and Computer Engineering

The Optical Sciences Center

Tucson, AZ 85721

[2] ABSTRACT: Optical storage systems offer the potential for drastically increased data transfer rates through the use of parallel access. The fidelity and capacity of these optical systems are impacted by the interfaces used to access the parallel data. In particular, the coding and signal processing components of the system must be designed with the 2D data format in mind. This research has focused on novel methods of coding both the object arms (e.g., interleaving) and the reference arms (e.g., apodizing) of holographic optical storage systems. Our research efforts have produced several significant results: (1) An information-theoretic methodology has been established for quantifying the performance of VH systems, (2) A multidimensional interleaving strategy has been developed for optimizing bit positions within a 2D channel, (3) An information-based design paradigm has been implemented for the design of data-bearing optical systems, and (4) Tradeoffs concerning the balance of noise reduction with storage density have been produced for both apodized and unapodized systems. Item (4) concerns work that is not yet published and a copy of an internal report describing this work is attached.

[3] TECHNICAL PROJECT SUMMARY: An outline of the research tasks completed during the period of this contract is given below. The detailed results associated with each of these tasks have been reported in numerous journal publications and student theses. A comprehensive list of these is also provided below.

1. Information theoretic capacity/density

- (a) identified noise and error sources relevant to VHM.
- (b) Discovered balance between number of pages and information per page.
- (c) Extended scalar information formalism to vector approximation.
- (d) Computed VHM capacity bounds for various random and systematic errors.

2. 2D interleaving

- (a) Formulated optimal interleaver in terms of topological framework.

- (b) Combined various codes with optimal and near-optimal interleaving.
- (c) Evaluated BER and capacity of interleaved systems over wide range of system parameters.
- (d) Experimental demonstration of interleaving and ECC.

### 3. Information-based design

- (a) Extended information-theoretic formalism to optical propagation and design.
- (b) Computed the information capacity of Fresnel propagation for various detection schemes.
- (c) Computed the information capacity of coherent imaging.
- (d) Investigated the optimization of pagewise mutual information and defined the information-theoretic space-bandwidth-product.
- (e) Defined new optimization metric for information-sensitive optical design.
- (f) Demonstrated utility of new design metric on various systems.

### 4. Apodization tradeoffs

- (a) Derived angular selectivity profile in terms of fundamental system parameters.
- (b) Studied relationship between apodization profile and crosstalk noise.
- (c) Derived the  $M/\#$  of an apodized VHM system.
- (d) Experimentally demonstrated use of various apodization profiles.

## [4] PUBLICATIONS:

- [1] W. C. Chou, B. M. King, and M. A. Neifeld, "Interleaving and Error Correction in Volume Holographic Memory Systems," *Applied Optics*, Vol. 37, pp. 6951–6968, 1998.
- [2] W. C. Chou, M. A. Neifeld, and R. Xuan "Information-based Optical Design for Binary-Valued Imagery," *Applied Optics*, Vol. 39, pp. 1731–1742, 1999.
- [3] B. M. King and M. A. Neifeld, "Sparse Modulation Coding for Increased Capacity in Volume Holographic Storage," *Applied Optics*, Vol. 35, pp. 6681–6688, 2000.

## [5] THESES:

- [1] Brian M. King, "Technical Advances in Volume Holographic Memories," Ph.D. thesis, University of Arizona Department of Electrical and Computer Engineering, granted 2001.

## CHAPTER 3

### Apodization

#### 3.1 Introduction

The key to achieving an enormous storage capacity in a volume holographic memory is the ability to multiplex a large number of holograms within the same physical volume. The choice of a multiplexing scheme dictates much of the system architecture necessary to allow extraction of the desired hologram from the collection. There are a large number of proposed multiplexing architectures,<sup>19,37-41</sup> each of which has its own unique advantages and disadvantages. We will primarily consider angular multiplexing but much of what is presented here can be easily applied to a variety of other multiplexing approaches.

A hologram is created by interfering the data-bearing object beam with a reference beam at a specific choice of the multiplexing parameter, say  $\psi_0$ . Later, when we wish to reconstruct the desired object beam, we use the reference beam corresponding to  $\psi_0$  resulting in a high-fidelity reconstruction of the object beam. As we perturb the multiplexing parameter, in general, the irradiance and quality of the reconstructed image decay. We wish to investigate in considerable detail precisely how the diffraction efficiency changes as we adjust the multiplexing parameter away from  $\psi_0$ .

When there are multiple holograms stored in the same memory, illumination with the desired reference beam reconstructs the desired page but it also produces contributions from all the other holograms albeit at very low diffraction

efficiencies relative to the desired page. Although with proper selection of the multiplexing spacing the hologram-to-hologram cross talk can be significantly reduced, it remains as a noise source that scales with the number of participating holograms. In the case of very high density storage, we expect that the cross talk level will limit acceptable retrieval of the desired data page. It is in this cross talk limited case that we wish to consider in this chapter.

We begin by reviewing Bragg diffraction for thick media and proceed to develop expressions for the diffraction efficiency and hologram-to-hologram cross talk in terms of the underlying system parameters specifically for angular multiplexing. The noise-to-signal (NSR) metric is introduced in sec. 3.5 to characterize the level of cross talk present. Reference beam apodization during recording and/or reconstruction is described as a technique to improve the NSR and improve both the multiplexing density of the memory and the total number of multiplexed holograms. In the last part of this chapter the relationship between apodization and  $M/\#$  is derived.

## 3.2 Bragg diffraction

The first step in understanding volume diffraction of the reference beam is to consider how a single location in the material responds to the incident optical wave. The first-order Born approximation<sup>7,42</sup> allows us to characterize the response at each point as a spherical scattering center with a scattering coefficient proportional to the local change in the material permittivity and amplitude of the illuminating wave. The field at a point in the output plane can then be

represented as the coherent superposition of the scattered wavelets from all the contributing points in the volume.

Note that the Born approximation is valid only for weak holograms. If the diffraction efficiency is significantly large, then the more rigorous coupled wave theory<sup>8</sup> must be applied. The small diffraction efficiency assumption can be thought of in two ways. First, that scattering from one location does not scatter again at some other location and two, the reference beam is not significantly attenuated due to the coupling of energy into the diffracted beam, *i.e.*, the energy lost in the reference beam due to the scattering is negligible.

By considering the reciprocal wavevector space (angular spectrum), we can represent the superposition of scattering sources in terms of a transfer function  $A(\vec{k}_i, \vec{k}_d)$  that provides the amplitude of the diffracted field with wavevector  $\vec{k}_d$  due to the component of the reference beam with incident wavevector  $\vec{k}_i$ .  $A(\vec{k}_i, \vec{k}_d)$  establishes a convenient mapping between input wavevectors and output diffracted wavevectors. The derivation can be found in refs. [42 and 43]. In the derivation it is assumed that the spatially varying material permittivity can be expressed as:

$$\epsilon(\vec{r}) = \epsilon_0 + \tilde{\epsilon}(\vec{r})e^{i\vec{K}_g \cdot \vec{r}} \quad (3.1)$$

where two conditions must be satisfied. First, the amplitude of the modulated permittivity must be much smaller than the bulk average permittivity:  $|\tilde{\epsilon}(\vec{r})| \ll \epsilon_0$ . The second requirement is that the spatial bandwidth of the permittivity modulation be much less than the grating frequency. Both conditions will be in practice satisfied for photorefractive holographic storage.

Accepting the previous assumptions, the wavevector transfer function can be written as:<sup>42,43</sup>

$$A(\vec{k}_i, \vec{k}_d) = \int_V \frac{\tilde{\epsilon}(\vec{r}) e^{i\vec{K}_g \cdot \vec{r}} E_i(\vec{r}) e^{i(\vec{k}_i - \vec{k}_d) \cdot \vec{r}}}{2i\sqrt{k^2 - k_{d,x}^2 - k_{d,y}^2}} d\vec{r} \quad (3.2)$$

where  $E_i(\vec{r})$  is the amplitude of the reference field at the position  $\vec{r}$  inside the scattering volume,  $V$ .

Note that if the reference beam only consists of one wavevector,  $\vec{k}_i$ , that  $A(\vec{k}_i, \vec{k}_d)$  defines the angular spectrum (in terms of the variable  $\vec{k}_d$ ) of the diffracted wave. We can then write the diffracted field as the inverse 2D Fourier transform of the wave's angular spectrum:

$$E_{out}(\vec{r}) = \int \int A(\vec{k}_i, \vec{k}_d) e^{i\vec{k}_d \cdot \vec{r}} dk_{d,x} dk_{d,y} \quad (3.3)$$

### 3.2.1 Ideal volume phase grating

Understanding diffraction from the ideal thick phase grating will serve as a starting point for the later more complicated developments. Consider the simple case where the permittivity modulation consists of an undamped single grating:  $\tilde{\epsilon}(\vec{r}) = 1$  and the grating vector,  $\vec{K}_g$ , is defined through the interference of an object monochromatic wave with wavevector  $\vec{k}_o$  and a recording reference wave with wavevector  $\vec{k}_r$ :

$$\vec{K}_g = \vec{k}_o - \vec{k}_r \quad (3.4)$$

If a crystal of dimensions  $W \times H \times L$  (refer to fig. 3.1) with negligible absorption (an ideal assumption) is illuminated with a reconstruction reference beam of wavevector  $\vec{k}_i$ , we wish to compute the amplitude of the diffracted field with

wavevector  $\vec{k}_d$ . By eq. 3.2, we know the amplitude of the diffracted field in the direction defined by  $\vec{k}_d$  is  $A(\vec{k}_i, \vec{k}_d)$  which can be simplified using the assumed ideal phase grating:

$$A(\vec{k}_i, \vec{k}_d) \propto \int_V \tilde{\epsilon}(\vec{r}) e^{i\vec{K}_g \cdot \vec{r}} E_i(\vec{r}) e^{i(\vec{k}_i - \vec{k}_d) \cdot \vec{r}} d\vec{r} \quad (3.5)$$

$$= \int_V e^{i\vec{K}_g \cdot \vec{r}} e^{i(\vec{k}_i - \vec{k}_d) \cdot \vec{r}} d\vec{r} \quad (3.6)$$

$$= \int_V e^{i(\vec{k}_o - \vec{k}_r) \cdot \vec{r}} e^{i(\vec{k}_i - \vec{k}_d) \cdot \vec{r}} d\vec{r} \quad (3.7)$$

$$= \int_V e^{i((\vec{k}_o - \vec{k}_d) + (\vec{k}_i - \vec{k}_r)) \cdot \vec{r}} d\vec{r} \quad (3.8)$$

$$= \int_V e^{-i\vec{\xi} \cdot \vec{r}} d\vec{r} \quad (3.9)$$

where the Bragg or momentum mismatch vector,  $\vec{\xi}$ , is defined as the vector difference between the grating, incident, and diffracted wavevectors:

$$\vec{\xi} \triangleq (\vec{k}_d - \vec{k}_o) + (\vec{k}_r - \vec{k}_i) \quad (3.10)$$

To satisfy the Bragg matching condition, the vector triplet  $(\vec{K}_g, \vec{k}_d, \vec{k}_i)$  should form a closed triangle such that:  $\vec{k}_d = \vec{K}_g + \vec{k}_i$ . When this occurs  $\vec{\xi}$  will be identically  $\vec{0}$ . The parentheses in eq. 3.10 are intended to suggest grouping the difference vectors between the object and diffracted wavevector and also the incident and recording reference wavevector. When the difference vectors are identically zero, there is strong diffraction; hence the ideal reconstruction of the original object beam. As a difference accrues between the wavevectors, the diffracted amplitude decreases. To understand conditions placed on the mismatch vector, we continue the simplification of eq. 3.9 by making the typical assumption that the transverse dimensions (width and height) of the volume holographic medium are much greater than the spatial bandwidth of the object beam. In this case



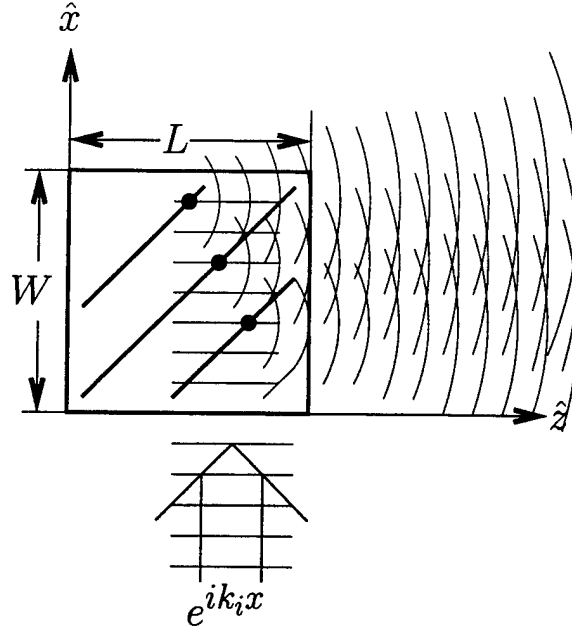


Figure 3.1: Crystal geometry and coordinate system for holographic recording in the 90 degree configuration. An example shows the superposition of scattered wavelets off of the phase grating.

the integrals over the transverse dimensions collapse into delta functions on the components of  $\vec{\xi}$  in the  $\hat{x}$  and  $\hat{y}$  directions. The  $\hat{z}$  direction remains producing:

$$A(\vec{k}_i, \vec{k}_d) \propto \int_V e^{-i\vec{\xi} \cdot \vec{r}} d\vec{r} \quad (3.11)$$

$$= \int_{-\infty}^{\infty} \int_{-\infty}^{\infty} \int_{z=0}^L e^{-i\vec{\xi} \cdot \vec{r}} dx dy dz \quad (3.12)$$

$$= \delta(\xi_x) \delta(\xi_y) \int_0^L e^{-i\xi_z z} dz \quad (3.13)$$

$$= \delta(\xi_x) \delta(\xi_y) \text{sinc}(\xi_z L/2) \quad (3.14)$$

where  $\text{sinc}(\varphi)$  is defined as  $\text{sinc}(\varphi) \triangleq \frac{\sin \varphi}{\varphi}$ .

### 3.2.2 Angular Selectivity

As an example, let the recording reference beam propagate at an angle  $\theta$  with respect to the  $\hat{x}$  axis. The reconstruction beam is at a slightly different angle:  $\theta + \Delta\theta$ . The Bragg mismatch in the  $\hat{z}$  direction is thus:

$$\xi_z = k \sin(\theta + \Delta\theta) - k \sin \theta \quad (3.15)$$

$$= k \Delta\theta \cos \theta \quad (3.16)$$

where the last step assumes  $\Delta\theta \ll \theta$  so that a first order Taylor series expansion of  $\sin(\theta + \Delta\theta)$  around  $\theta$  is valid. The amplitude of the diffracted field in the direction of the object wavevector for a reference beam detuned by a small angle,  $\Delta\theta$  is:

$$A(\vec{k}_i, \vec{k}_d) = \text{sinc}(\xi_z L/2) \quad (3.17)$$

$$= \text{sinc}\left(\frac{k \Delta\theta L}{2} \cos \theta\right) \quad (3.18)$$

$$= \text{sinc}\left(\frac{\pi \Delta\theta}{\Delta\Theta}\right) \quad (3.19)$$

where  $\Delta\Theta$  is the null spacing of the sinc function. Note that in terms of the wavelength,  $\Delta\Theta$  is:

$$\Delta\Theta = \frac{\lambda}{L \cos \theta} \quad (3.20)$$

If  $\lambda = 0.5 \mu\text{m}$ ,  $L = 1 \text{ cm}$ ,  $\theta = 0$  then  $\Delta\Theta = 5 \times 10^{-5}$  radians or  $2.86 \times 10^{-3}$  degrees (measured externally to the crystal). Fig. 3.2 plots the angular selectivity for this example.

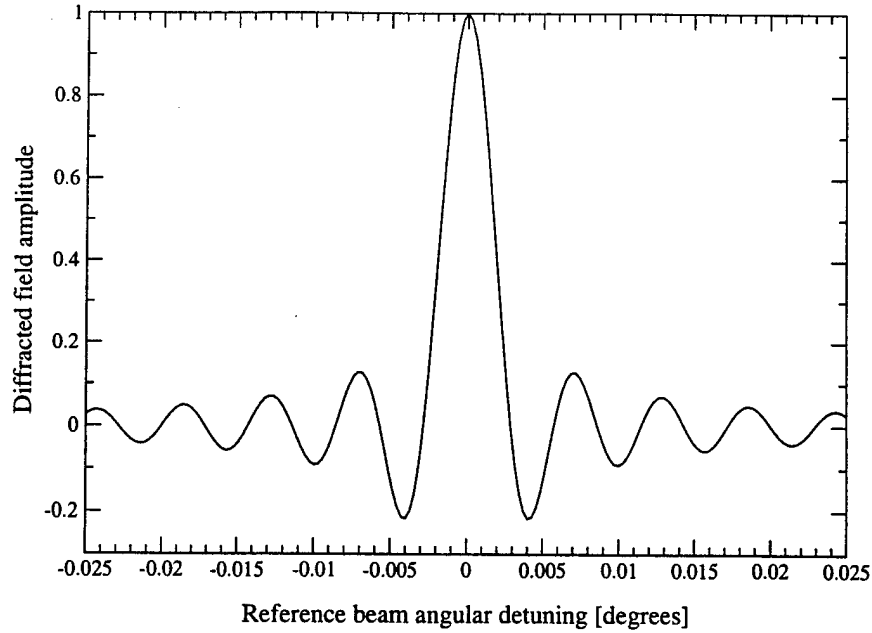


Figure 3.2: Bragg angular selectivity for a 1 cm long crystal with  $\lambda = 0.5 \mu\text{m}$  and a recording reference beam angle of 0 degrees.

### 3.3 Bragg Selectivity Function

The general extension of the angular selectivity is the Bragg selectivity function (BSF). It yields the diffraction efficiency as the reference beam is detuned away from the value used during recording. The detuning may occur due to changes in wavelength ( $\lambda$ -mux) or rotations of the medium (peristrophic-mux), or a variety of others possibilities. Regardless, in every case it is the change in the Bragg momentum vector,  $\xi$ , that matters.

In the case of angular multiplexing, we saw that the transverse components of the mismatch were constrained to be zero. In this instance, the BSF is reduced to a one-dimensional function of  $\xi_z$ , the momentum mismatch nominally in the direction of the object wavevector. The diffraction efficiency is thus the

BSF evaluated at  $\xi_z$ . The strict relationship between  $\xi_z$  and the reference beam angle depends on the specific interacting object-reference grating vector, but the dependence is slight. Writing the relation as in eq. 3.16, is accurate to third order for small deviations from  $\theta$ .

### 3.3.1 Material Effects and the BSF

The ideal case assumed the spatial modulation envelope of the permittivity to be constant. In practice, this does not occur due to the presence of material absorption among other things.

In this section we wish to incorporate the attenuated power profiles of the object and reference beams during recording and also on reconstruction. We also wish to assume an apodized form for the reference plane wave as described next.

During reconstruction we choose  $R(z)$  to be the apodized field profile of the reference beam. It is defined such that  $\max_z |R(z)| = 1$ , thus the peak magnitude of the wave is  $R_0$ . During recording, the reference beam is defined as:

$$E_r(\vec{r}) = W_0 W(z) e^{i\vec{k}_r \cdot \vec{r}} \quad (3.21)$$

where a small reference beam angle is assumed in order to ignore the geometric shadowing effect in  $W(z)$ . This is valid to third order deviations in the reference beam angle away zero degrees.

The reference beam interferes with each plane wave component in the object beam. We model each component in electric field as:

$$E_o(\vec{r}) = S_0 e^{i\vec{k}_o \cdot \vec{r}} \quad (3.22)$$

As is common in the literature, we assume all inferred angles, wavelengths, and wavevectors are specified inside the material. We tacitly assume that the space surrounding the hologram is index matched to the crystal. If external angles are desired, then Snell's law must be applied.

On reconstruction, we use a new reference beam (the same as the recording beam for Bragg-matched conditions) of:

$$E_i(x=0, y, z) = R_0 R(z) e^{i\vec{k}_i \cdot \vec{r}} \quad (3.23)$$

The reference beam diffracts through the volume hologram for  $x \in [0, W]$  and  $z \in [0, L]$ . As it propagates nominally in the  $\hat{x}$  direction, it will be attenuated due to the crystal absorption. The reference beam at a point  $\vec{r}$  in the medium is expressed as:

$$E_i(\vec{r}) = R_0 R(z) e^{-\frac{\alpha}{2}x} e^{i\vec{k}_i \cdot \vec{r}} \quad (3.24)$$

where  $\alpha$  is the irradiance bulk absorption coefficient. The same relationship holds for the recording reference beam, the object wave, and the diffracted wave. Note we will assume only phase holograms so there is no spatial modulation of the absorption coefficient.

The permittivity modulation of the hologram results indirectly from the space charge field established during the holographic exposure. The fast fringe patterns in irradiance are mimicked by phase-shifted spatial electric fields established by electrons bound in doped deep impurity traps. The linear electro-optic effect then produces the permittivity modulation from the space charge field.<sup>44</sup> For a small amplitude modulation of the permittivity, the material index of refraction approximately duplicates the spatial distribution. For the 90 degree angular

multiplexing configuration in LiNbO<sub>3</sub>, the c-axis is oriented at 45 degrees to the  $x$ - $z$  plane to maximize the projection of the grating vector on the electro-optic coefficient,  $r_{13}$ . In this case, the permittivity modulation is:

$$\tilde{\epsilon}(\vec{r})e^{i\vec{K}_g \cdot \vec{r}} = -\epsilon_0 n_o^4 r_{13} E_1(\vec{r}) \quad (3.25)$$

where  $n_o$  is the ordinary index of refraction (around 2.286 for  $\lambda = 514$  nm) and  $E_1(\vec{r})$  is the space charge field generated during the recording process.

Combining eqs. 3.2 and 3.25 we compute the amplitude of the diffracted plane wave component traveling with the correct object wavevector,  $\vec{k}_o$ . The deviation of the reconstruction reference beam from the recording beam is captured in the momentum mismatch term  $\vec{\xi}$ :

$$E_d(\vec{\xi}) = \int_V R_0 R(z) e^{-\frac{\alpha}{2}(L-z+x)} e^{i(\vec{k}_i - \vec{k}_o) \cdot \vec{r}} \tilde{\epsilon}(\vec{r}) e^{i\vec{K}_g \cdot \vec{r}} d\vec{r} \quad (3.26)$$

$$= -\epsilon_0 n_o^4 r_{13} \int_V R_0 R(z) e^{-\frac{\alpha}{2}(L-z+x)} e^{i(\vec{k}_i - \vec{k}_o) \cdot \vec{r}} E_1(\vec{r}) d\vec{r} \quad (3.27)$$

$$= -\epsilon_0 n_o^4 r_{13} \int_V R_0 R(z) e^{-\frac{\alpha}{2}(L-z+x)} e^{i(\vec{k}_r - \vec{k}_o) \cdot \vec{r}} E_1(\vec{r}) e^{-i\vec{\xi} \cdot \vec{r}} d\vec{r} \quad (3.28)$$

We see that the diffracted amplitude can be represented as a three-dimensional Fourier transform with  $\vec{r}$  and  $\vec{\xi}$  forming a reciprocal vector pair. Ignoring some of the normalization constants we can write the relationship as:

$$E_d(\vec{\xi}) \propto \text{FT} \left[ R_0 R(z) e^{-\frac{\alpha}{2}(L-z+x)} e^{i(\vec{k}_r - \vec{k}_o) \cdot \vec{r}} E_1(\vec{r}) \right] \quad (3.29)$$

Remembering for the case of angular multiplexing that the transverse mismatch components  $\xi_x$  and  $\xi_y$  must be identically zero, we can simplify the relationship into a one-dimensional Fourier transform pair:

$$\begin{aligned} E_d(\xi_z) &\propto \int_0^H \int_0^W e^{-\frac{\alpha}{2}x} e^{i(\vec{k}_r - \vec{k}_o) \cdot \hat{x}} E_1(\vec{r} \cdot \hat{x}) dx dy \cdot \\ &\quad \text{FT} \left[ R_0 R(z) e^{-\frac{\alpha}{2}(L-z)} e^{i(\vec{k}_r - \vec{k}_o) \cdot \hat{z}} E_1(\vec{r} \cdot \hat{z}) \right] \end{aligned} \quad (3.30)$$

We define the Bragg selectivity function,  $\eta(\xi_z)$ , and the Bragg profile function (BPF),  $\Gamma(z)$  from eq. 3.30 as:

$$\begin{aligned} \eta(\xi_z) &= \int_0^H \int_0^W e^{-\frac{\alpha}{2}x} e^{i(\vec{k}_r - \vec{k}_o) \cdot \hat{x}} E_1(\vec{r} \cdot \hat{x}) dx dy \cdot \\ &\quad \text{FT} \left[ R_0 R(z) e^{-\frac{\alpha}{2}(L-z)} e^{i(\vec{k}_r - \vec{k}_o) \cdot \hat{z}} E_1(\vec{r} \cdot \hat{z}) \right] \end{aligned} \quad (3.31)$$

$$= \text{FT} [\Gamma(z)] \quad (3.32)$$

The BSF and BPF will be simplified once we have a more specific form for the space charge field,  $E_1(\vec{r})$ . The first step in finding  $E_1(\vec{r})$  is to compute the modulation depth established during recording.

### 3.3.2 Modulation depth

The space charge field will be proportional to the interference grating formed between the apodized reference beam (defined in eq. 3.21) and one of the plane wave components present in the object beam (eq. 3.22).

Interfering two plane waves with wavevectors  $\vec{k}_o$  and  $\vec{k}_r$  produces an interference pattern with a grating vector of:

$$\vec{K}_g = \vec{k}_o - \vec{k}_r \quad (3.33)$$

The local irradiance at a location  $\vec{r}$  in the crystal is:

$$I(\vec{r}) \propto |E_o(\vec{r})e^{-\frac{\alpha}{2}z} + E_r(\vec{r})e^{-\frac{\alpha}{2}x}|^2 \quad (3.34)$$

$$= I_0(\vec{r}) + E_o(\vec{r})E_r^*(\vec{r})e^{-\frac{\alpha}{2}(z+x)} + E_r(\vec{r})E_o^*(\vec{r})e^{-\frac{\alpha}{2}(z+x)} \quad (3.35)$$

$$= I_0(\vec{r}) \left( 1 + \frac{S_0 W_0 W(z)e^{-\frac{\alpha}{2}(z+x)}}{I_0(\vec{r})} e^{i\vec{K}_g \cdot \vec{r}} + \frac{S_0 W_0 W^*(z)e^{-\frac{\alpha}{2}(z+x)}}{I_0(\vec{r})} e^{-i\vec{K}_g \cdot \vec{r}} \right) \quad (3.36)$$

$$= I_0(\vec{r}) \left( 1 + m(\vec{r})e^{i\vec{K}_g \cdot \vec{r}} + m^*(\vec{r})e^{-i\vec{K}_g \cdot \vec{r}} \right) \quad (3.37)$$

$$m(\vec{r}) = \frac{S_0 W_0 W(z)e^{-\frac{\alpha}{2}(z+x)}}{I_0(\vec{r})} \quad (3.38)$$

where  $I_0(\vec{r})$  is defined as:

$$I_0(\vec{r}) = |E_o(\vec{r})|^2 e^{-\alpha z} + |E_r(\vec{r})|^2 e^{-\alpha x} \quad (3.39)$$

$$= S_0^2 e^{-\alpha z} + W_0^2 |W(z)|^2 e^{-\alpha x} \quad (3.40)$$

For short exposure times the space charge field amplitude will grow linearly with the modulation depth  $m(\vec{r})$ :

$$E_1(\vec{r}; t) \propto m(\vec{r})e^{i\vec{K}_g \cdot \vec{r}} t \quad (3.41)$$

Notice from eq. 3.37 that there are possibly two interference gratings formed. One that is Bragg-matched to reconstruction with the recording beam ( $m(\vec{r})$ ) and a second matched to reconstruction with the phase conjugate of the recording wave ( $m^*(\vec{r})$ ). In a thick hologram, the conjugate wave will not diffract when reconstructing with a reference beam propagating in the approximate same direction as the original reference beam, allowing us to ignore the  $m^*(\vec{r})$  grating term.



### 3.3.3 Bragg Profile Function

From the modulation depth given in eqs. 3.36 and 3.37, and the grating amplitude (eq. 3.41), we can simplify the Bragg profile function:

$$\Gamma(z) \propto \int_0^H \int_0^W R_0 R(z) e^{-\frac{\alpha}{2}(L-z+x)} e^{i(\vec{k}_r - \vec{k}_o) \cdot \vec{r}} E_1(\vec{r}) dx dy \quad (3.42)$$

$$= \int_0^H \int_0^W R_0 R(z) e^{-\frac{\alpha}{2}(L-z+x)} e^{-i\vec{K}_g \cdot \vec{r}} m(\vec{r}) e^{i\vec{K}_g \cdot \vec{r}} dx dy \quad (3.43)$$

$$= H \int_0^W R_0 R(z) e^{-\frac{\alpha}{2}(L-z+x)} m(x, z) dx \quad (3.44)$$

$$= H \int_0^W \frac{S_0 R_0 W_0 R(z) W(z) e^{-\alpha x} e^{-\frac{\alpha}{2}L}}{S_0^2 e^{-\alpha z} + W_0^2 |W(z)|^2 e^{-\alpha x}} dx \quad (3.45)$$

$$= H \left( \frac{S_0}{W_0} \right) \int_0^W \frac{R_0 R(z) W(z) e^{-\alpha x} e^{-\frac{\alpha}{2}L}}{(S_0/W_0)^2 e^{-\alpha z} + |W(z)|^2 e^{-\alpha x}} dx \quad (3.46)$$

$$= H \left( \frac{S_0}{W_0} \right) R_0 R(z) W(z) e^{-\frac{\alpha}{2}L} \int_0^W \frac{e^{-\alpha x} dx}{(S_0/W_0)^2 e^{-\alpha z} + |W(z)|^2 e^{-\alpha x}} \quad (3.47)$$

$$= H \left( \frac{S_0}{W_0} \right) \frac{R_0 R(z) e^{-\frac{\alpha}{2}L}}{|W(z)|} \left[ W + \frac{1}{\alpha} \ln \frac{|W(z)|^2 + (S_0/W_0)^2 e^{-\alpha z}}{|W(z)|^2 + (S_0/W_0)^2 e^{-\alpha z} e^{\alpha W}} \right] \quad (3.48)$$

$$= H \left( \frac{S_0}{W_0} \right) \frac{R_0 R(z) e^{-\frac{\alpha}{2}L}}{|W(z)|} \left[ W + \frac{1}{\alpha} \ln \frac{1 + A(z) e^{-\alpha z}}{1 + A(z) e^{-\alpha(z-W)}} \right] \quad (3.49)$$

$$A(z) \triangleq (S_0/W_0)^2 / |W(z)|^2 \quad (3.50)$$

The integral in eq. 3.47 can be solved in closed form as long as  $W(z) \neq 0$ :

$$\int_0^W \frac{e^{-\alpha x}}{C e^{-\alpha x} + D} dx = \frac{1}{\alpha C} [\alpha W + \ln(C + D) - \ln(C + D e^{\alpha W})] \quad (3.51)$$

It is clear that when  $W(z) = 0$  the integral simplifies to:

$$\int_0^W \frac{e^{-\alpha x} dx}{(S_0/W_0)^2 e^{-\alpha z} + |W(z)|^2 e^{-\alpha x}} = \frac{1 - e^{-\alpha W}}{(S_0/W_0)^2 \alpha e^{-\alpha z}} \quad (3.52)$$

$A(z)$  is the local apodized beam ratio. The BPF and BSF defined in eqs. 3.31 and 3.32 can now be expressed in their full form:

$$\begin{aligned}\eta(\xi_z) &\propto \int_0^L \left( \frac{S_0}{W_0} \right) \frac{R_0 R(z)}{|W(z)|} \left[ W + \frac{1}{\alpha} \ln \frac{1 + A(z)e^{-\alpha z}}{1 + A(z)e^{-\alpha(z-W)}} \right] e^{-i\xi_z z} dz \quad (3.53) \\ &= \text{FT} [\Gamma(z)] , \quad (3.54)\end{aligned}$$

where  $\Gamma(z)$  is defined to be zero outside the interval  $[0, L]$  and also for any  $z$  such that  $W(z) = 0$ .

We refer to  $\Gamma(z)$  as the Bragg profile function (BPF) because it is the Fourier reciprocal function to the BSF. Because the BPF is limited to a spatial extent of  $L$ , we see an immediate consequence is that the BSF can not provide a narrower main lobe than  $\xi_0 = 2\pi/L$ . This can be made clearer by examining the Fourier transform pair:

$$\Gamma(z) = 1 \quad (3.55)$$

$$\eta(\xi_z) = \text{sinc}(\xi_z L/2) \quad (3.56)$$

$\xi_0$  represents the smallest null spacing possible for the given length  $L$ . It thus establishes a practical minimum separation between successive holograms. Comparing this result to sec. 3.2.1 we see that this case occurs when the overall system acts like an ideal thick phase hologram.

To provide some real numbers, consider angular multiplexing in a  $1 \times 1 \times 1$  cm<sup>3</sup> crystal. The ideal BSF for the  $\theta = 0$  page has periodic nulls at integer multiples of  $\Delta k = \sin^{-1}(\lambda/L)$ . This represents a nearly constant angular spacing of  $\lambda/L \approx 5 \times 10^{-5}$  radians or  $2.86 \times 10^{-3}$  degrees. There can be up to 14,000 multiplexed holograms in a  $\pm 20$  degree span. Of course, such a large angular

range places additional non-trivial design requirements on the optical system implementation which we tacitly assume have been adequately satisfied (in this chapter at least).

### 3.4 Apodization Theory

The periodic nulls of the BSF are not actually nulls in reality due to the presence of absorption. Absorption can not be eliminated as it is one of the key operating mechanisms responsible for the photorefractive effect. The first few absorption-corrupted nulls can often produce an unacceptably large diffraction efficiency leading to significant interpage crosstalk. In practice it is common to reduce the crosstalk by storing pages not on the first nulls of the BSF but on the second, third, or fourth. This solution markedly reduces the multiplexing density.

Another technique that has been proposed to reduce the crosstalk without sacrificing the density is apodization.<sup>13,17,45-47</sup> The reference beam is shaped during recording and reconstruction in order to provide a suitably improved BSF. Apodization can be applied in three ways:

1. during recording only:  $R(z) = 1$
2. during reconstruction only:  $W(z) = 1$
3. during both recording and reconstruction

Figure 3.3 shows the apodization profiles for (a) no apodization, (b) reconstruction only, and (c) recording only, where the apodizers are chosen to flatten out their associated  $\Gamma(z)$ . Figure 3.4 shows  $\Gamma(z)$  for the three apodizers. For these

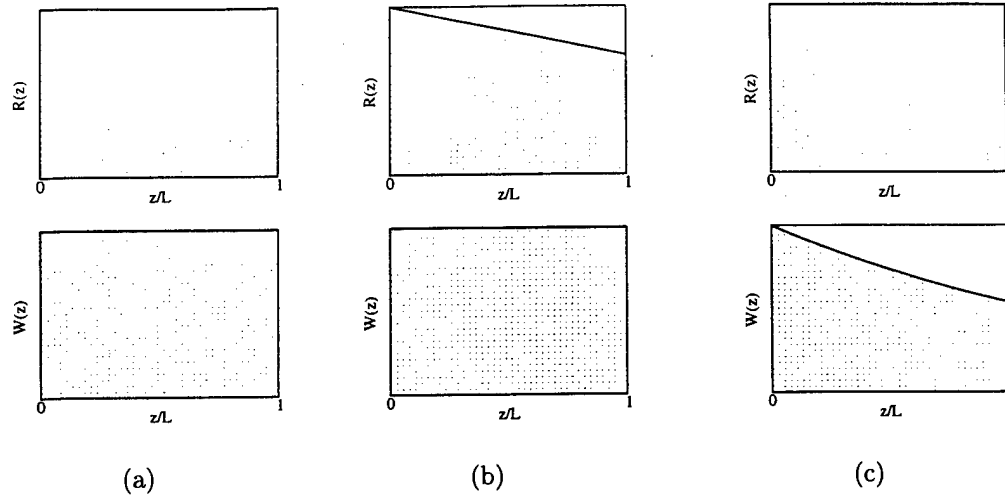


Figure 3.3: Apodizer profiles for (a) no apodization (b) reconstruction beam apodization (c) recording beam apodization.

figures the assumed beam ratio is 1,  $L = W = H = 1$  cm, and  $\alpha = 0.73$  cm<sup>-1</sup>. Notice that the reconstruction apodizer merely corrects for the nearly constant slope present in the no apodization case. The recording apodizer accounts for the exponential absorption of the signal beam as it propagates in the  $+z$  direction.

The BSF for the three apodizers are shown in figure 3.5. The non-flat profile of the no apodization  $\Gamma(z)$  results in a relative amplitude diffraction efficiency of 5.817% and 2.894% at the first and second nulls, respectively. Reconstruction apodization corrects most of this by flattening out  $\Gamma(z)$ . Note that recording apodization can precisely flatten  $\Gamma(z)$  and recover the perfect Bragg nulls.

During reconstruction, all the pages in the memory contribute a small diffracted component superimposed with the Bragg-matched page. This coherent superposition constitutes a data-dependent coherent field noise source that we refer to as interpage crosstalk. When no apodization is performed the nearby few

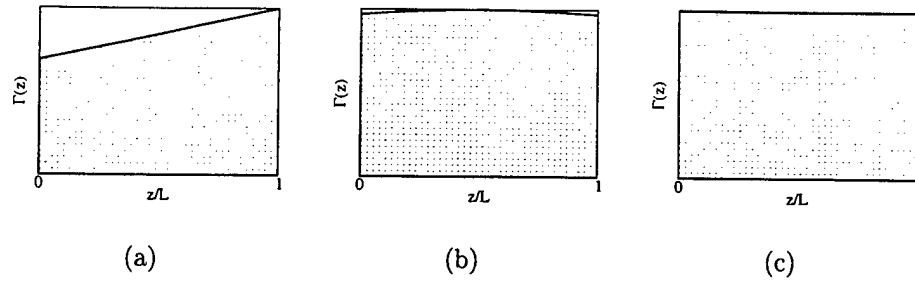


Figure 3.4: Effective BSF Fourier transform kernel for (a) no apodization (b) reconstruction beam apodization (c) recording beam apodization.

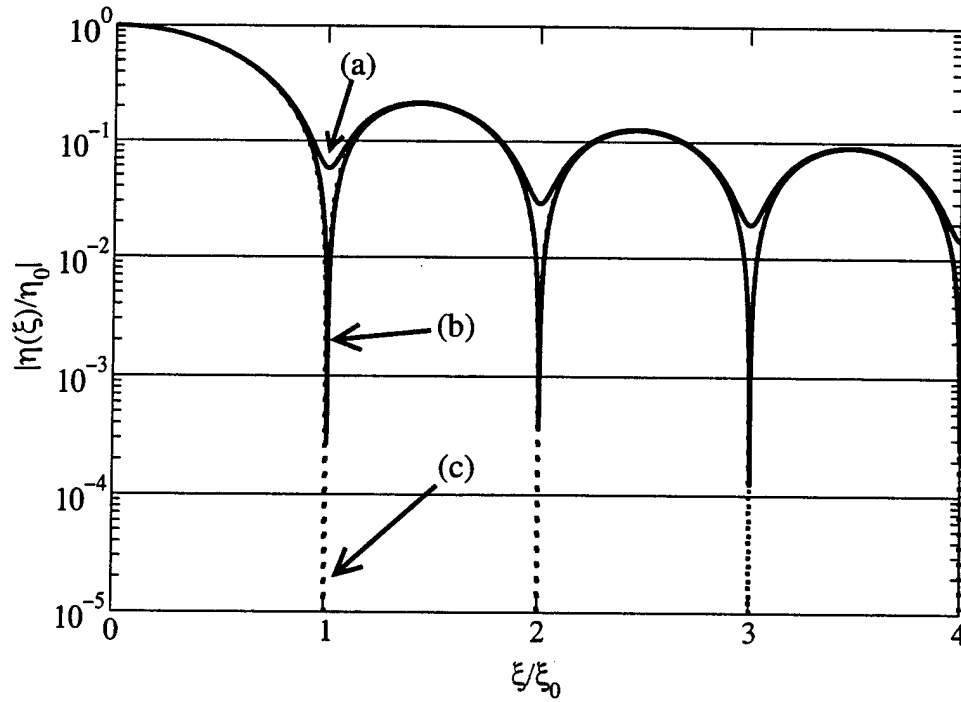


Figure 3.5: Normalized amplitude diffraction efficiency versus normalized multiplexing detuning for (a) no apodization (b) reconstruction beam apodization (c) recording beam apodization.

multiplexed pages dominate the crosstalk noise and force a loss in multiplexing density in order to allow reliable page retrieval. The above proposed recording or reconstruction apodizers strongly reduce the cross talk noise, but there is an associated loss in diffraction efficiency due to apodization; apodization lowers the system  $M/\#$  as is discussed later in sec. 3.6.

### 3.4.1 Experiment

To verify that we could modify the Bragg selectivity function by changing the reference beam profile, we conducted some experiments. The optical setup was constructed in a 90 degree angular-multiplexing configuration. A Newport rotation stage (0.001 deg accuracy) was used for coarse angular selection as well as for angular scans at an approximate constant velocity. A New Focus picomirror mount (0.1 mdeg accuracy) was used for fine angular control.

The photorefractive crystal was placed 3 mm behind the Fourier plane of the object arm, resulting in Fresnel holograms. For this experiment, a 5 mm  $\times$  5 mm  $\times$  5mm KNSBN crystal was used. The crystal was chosen for its fast recording time and low absorption ( $\alpha = 0.55 \text{ cm}^{-1}$ ).

Figs. 3.6 and 3.7 show the reference beam profile, hologram modulation depth, and Bragg selectivity function for rectangular and triangular apodization. The non-uniform (decaying exponential) modulation depth in the rectangular apodization clearly shows the effect of the crystal absorption. The "filling-in" of the Bragg nulls as a result is likewise apparent in fig. 3.6c. For the case of triangle apodization, there are no solid conclusions. The periodic Bragg nulls can not clearly be

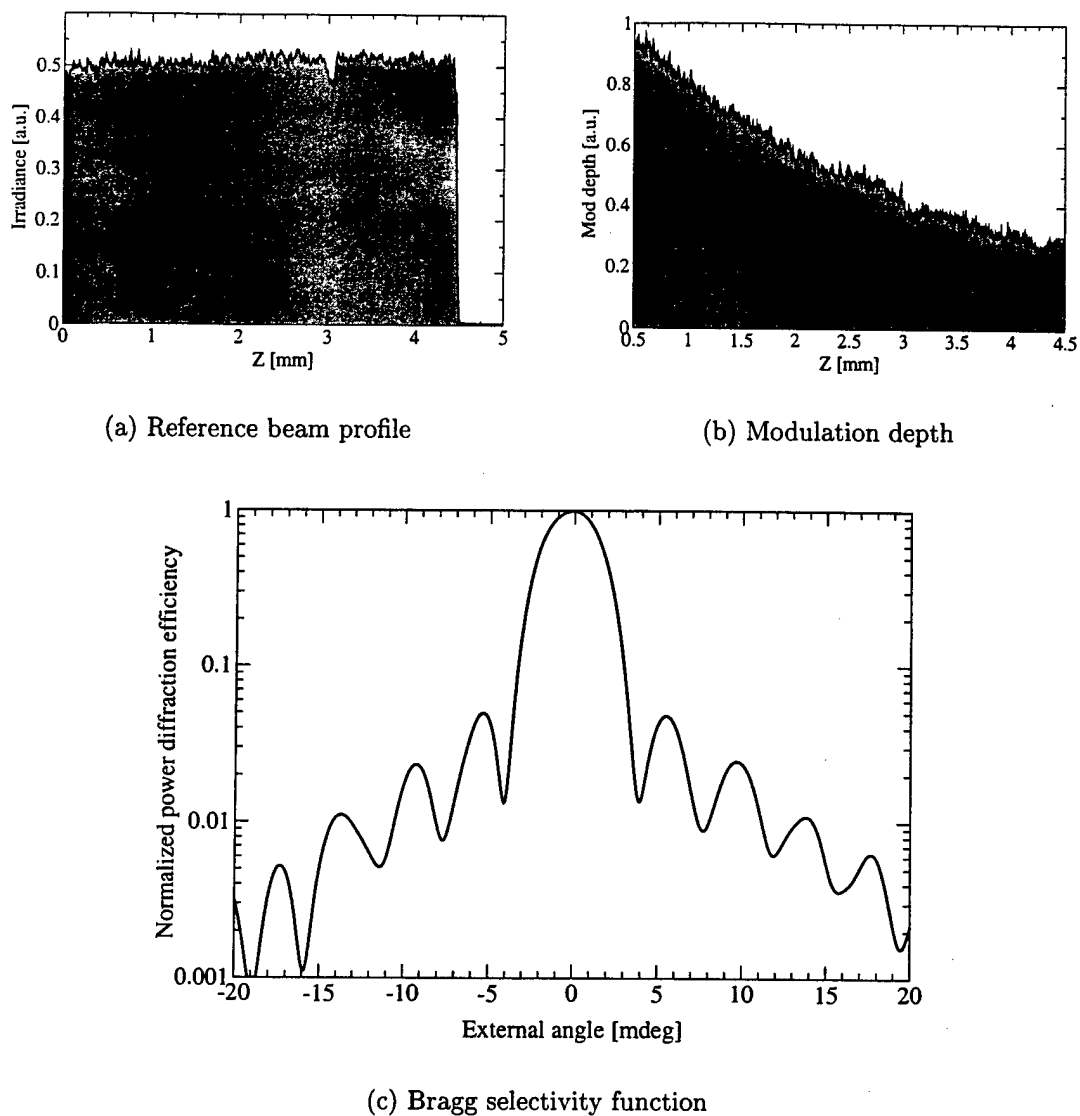
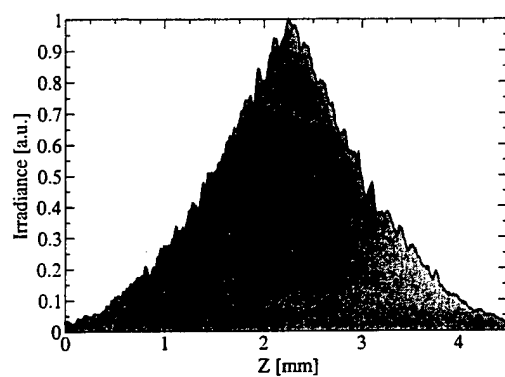
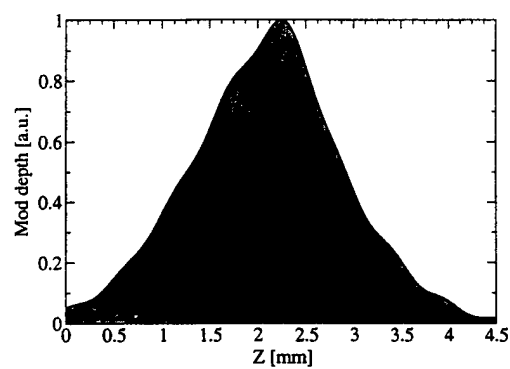


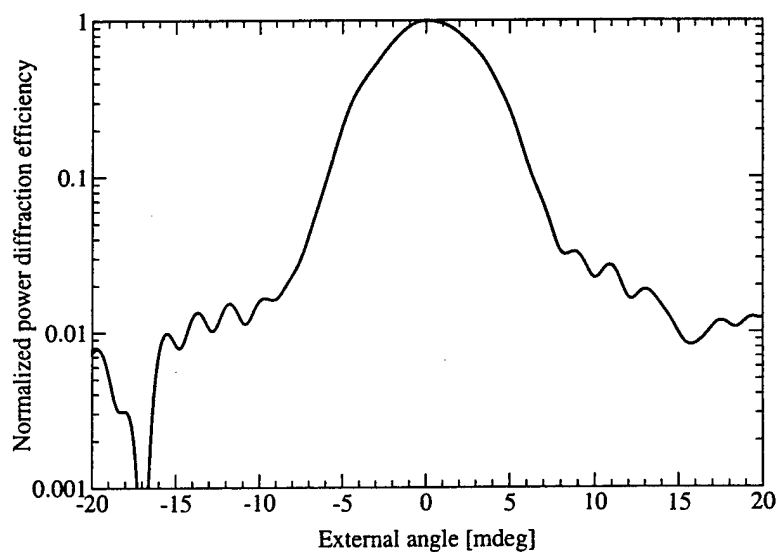
Figure 3.6: Rectangle apodization. Experimental (a) reference beam profile, (b) resulting modulation depth, and (c) Bragg selectivity function in a 5mm sample of KNSBN. The recording beam ratio was 10:1.



(a) Reference beam profile



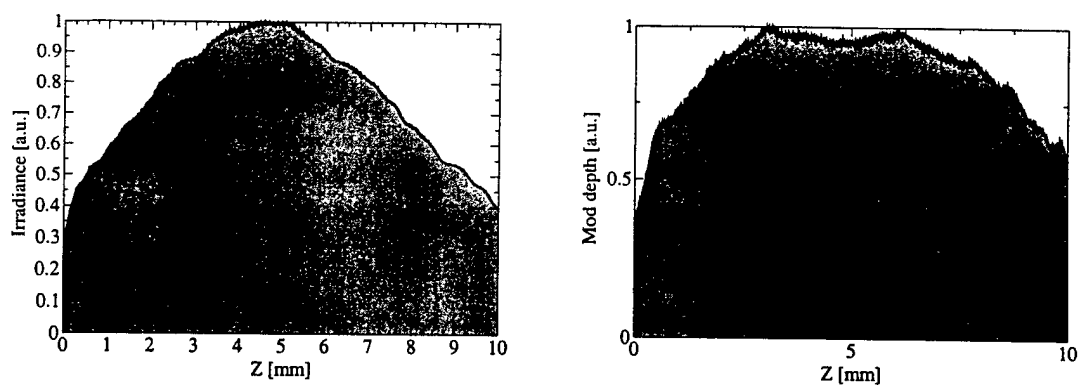
(b) Modulation depth



(c) Bragg selectivity function

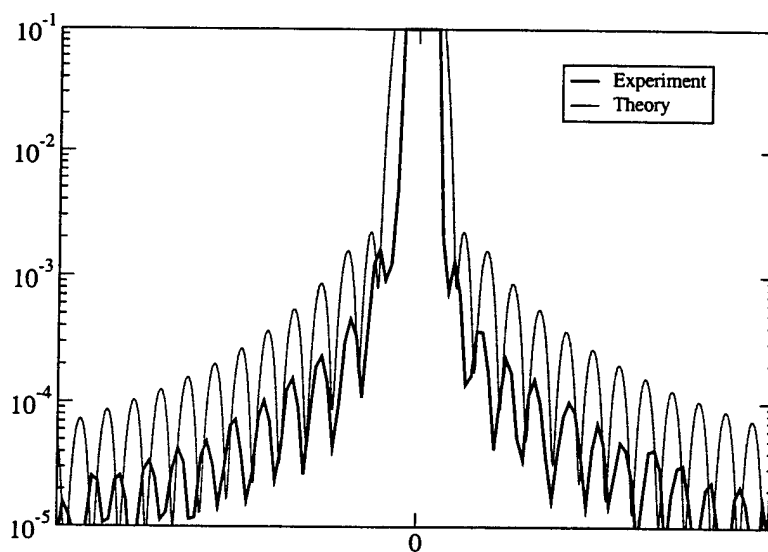
Figure 3.7: Triangle apodization. Experimental (a) reference beam profile, (b) resulting modulation depth, and (c) Bragg selectivity function in a 5mm sample of KNSBN. The recording beam ratio was 10:1.





(a) Reference beam profile

(b) Modulation depth



(c) Bragg selectivity function

Figure 3.8: Gaussian apodization. Experimental (a) reference beam profile, (b) resulting modulation depth, and (c) Bragg selectivity function in a 1cm sample of  $\text{Fe:LiNbO}_3$ . The recording beam ratio was 10:1.

distinguished. Though, we do see the profile and modulation depth behave as we expect.

Fig. 3.8 shows the results of using no intentional apodization (implicitly a Gaussian apodizer). The available high beam power allows very good resolution on the sidelobes of the BSF. On top of the experimental curve is plotted the theoretical prediction for the 1 cm Fe:LiNbO<sub>3</sub> crystal with absorption coefficient  $3.8 \text{ cm}^{-1}$ .

### 3.4.2 Crosstalk noise sources

So far we have discussed apodization with respect to the effects of the crystal absorption during the recording and readout processes. Even when the BSF is the ideal sinc function, there will still be an intrinsic amount of cross talk that grows with the number of pages in the memory. It is a directly a result of the non-zero angular span of object wavevectors in the  $\hat{x}$  direction, as well as a small change in the null spacing with increasing off-axis reference beam angles. For small object spatial bandwidths and reference angular range, this crosstalk can be negligibly small. But when the number of multiplexed holograms is very large, then the additive field noise will offer a significant contribution.

In addition to intrinsic cross talk noise, there are primarily two other mechanisms by which cross talk can limit the system performance. First, if absorption is not corrected, the neighboring holograms will cross talk significantly. As discussed earlier, besides apodization, this effect can be reduced by spacing the holograms on a larger angular spacing, but this may not be a good system level

choice due to the extra reference beam angular bandwidth that is sacrificed. The larger angles also increase the effect of the intrinsic crosstalk.

A second cross talk source is a consequence of non-ideal angular pointing accuracy in the reference beam. Errors in the reference beam angle will decrease the diffraction efficiency of the desired page and increase the cross talk from the other holograms. The cross talk is very sensitive to angular beam jitter, and therefore very small pointing errors will quickly magnify the cross talk levels.

We propose apodization as a technique that:

1. compensates for the non-uniform grating profile (and hence restore the sinc nulls)
2. increases tolerance to angular jitter by decreasing the slope of the BSF around the nulls

We measure the effectiveness of apodization by introducing the noise-to-signal ratio (NSR) which characterizes the cross talk noise by the first and second moments on the detection plane irradiance signal. We discuss a variety of apodization shapes to reduce the NSR in the presence of intrinsic cross talk noise, absorption, jitter, and both a coherent and incoherent page-to-page phase model. Afterwards in sec. 3.6, we derive the relationship between apodization and the holographic system metric  $M/\#$ .

### 3.5 Noise-to-Signal Ratio

The diffracted field present at the detection plane can be written as a superposition of every stored hologram weighted by their diffraction efficiency. For

retrieval of page  $j$  we write the field amplitude as:

$$E = \sum_{m=-M_1}^{M_1} \eta(\xi_z(m; j)) E_O^{(m)} e^{i\phi_m} \quad (3.57)$$

where the shorthand notation of  $\xi(m; j)$  refers to the component of the Bragg mismatch vector in the  $\hat{z}$  direction between pages  $m$  and  $j$ . The large transverse dimensions (with respect to the spatial bandwidth of the object beam) require the other components of  $\vec{\xi}$  to be identically zero. This introduces a small shift in the diffracted images that we can ignore; however it also imparts a small deviation to  $\xi_z$  as well, which is accounted for in our simulation model.

The last term in eq. 3.57 may or may not be present depending on the model. The term  $e^{i\phi_m}$  represents a random phase present upon retrieval of a page. When we incorporate this term, we will refer to the cross talk as incoherent (as the average effect of the term is to average out the cross talk). The phase is assumed to be uniform over the full range of  $2\pi$ . When the term is not present, the cross talk is said to be coherent.

For Fourier holograms, we can write the object beam as a collection of plane waves with direction cosines corresponding to the associated pixel location:

$$E_O^{(m)} = a_{mlp} e^{i\vec{k}_{lp} \cdot \vec{r}} \quad (3.58)$$

$$\vec{k}_{lp} = k(\cos \alpha_p \cos \beta_l \hat{z} - \sin \alpha_p \cos \beta_l \hat{y} - \sin \beta_l \hat{x}) \quad (3.59)$$

where  $\alpha_p$  and  $\beta_l$  are the direction angles between the pixel at location  $(l, p)$  on the SLM and the center of the Fourier transform lens a distance  $f$  away from the SLM.  $a_{mlp}$  is the SLM pixel value for page  $m$ , pixel location  $(l, p)$ . In this chapter we will only consider a binary amplitude SLM so  $a_{mlp}$  is either 0 or 1.

The Bragg mismatch vector associated with reconstructing the grating corresponding to page  $m$  and pixel  $(l, p)$  ( $\vec{k}_r = \vec{k}^{(m)}$ ,  $\vec{k}_o = \vec{k}_{lp}$ ), using the reference beam for page  $j$  ( $\vec{k}_i = \vec{k}^{(j)}$ ) is:

$$\vec{\xi} = \vec{k}_o - \vec{k}_d + \vec{k}_i - \vec{k}_r \quad (3.60)$$

$$= \vec{k}_{lp} - \vec{k}_d + \vec{k}^{(j)} - \vec{k}^{(m)} \quad (3.61)$$

where the requirements for non-zero diffraction imply that  $\xi_x = 0$  and  $\xi_y = 0$ . In order to achieve this, a slight rotation of  $\vec{k}_d$  is necessary which imparts a small change to  $\xi_z$ . This slight dependence on the  $\hat{x}$  component of the object wavevector,  $\vec{k}_{lp}$  is responsible for different columns on the same page having slightly different mismatches and hence slightly different cross talk values. We can ignore the  $y$  dependence of the mismatch as it is in the degenerate direction (with an exception for fractal multiplexing). As a result of this degeneracy, all the pixels in the same column on the same object page will have similar cross talk properties. The amplitude of each individual cross talk contribution is just the Bragg selectivity function evaluated at  $\xi_z$ .

The important thing to note is that the cross talk properties vary across columns of pixels in the detection plane as well as from page to page. Previous studies<sup>13,46,48</sup> have analyzed the cross talk over all pages and all columns and found that the worst cross talk occurs at approximately  $m = M_r \triangleq \pm 0.9M_1$  for the column of pixels with the largest wavevector component in the  $\hat{x}$  direction. We will refer to all cross talk measurements with respect to this reference location of page  $M_r$ . The diffracted field,  $E$ , at a pixel in the detection plane for the worst

case cross talk position can be written as:

$$E \propto \sum_{m=-M_1}^{M_1} a_{mlp} \eta(\xi_z) e^{i\phi_m} \quad (3.62)$$

$$\xi_z = (\vec{k}_{lp} - \vec{k}_d + \vec{k}^{(M_r)} - \vec{k}^{(m)}) \cdot \hat{z} \quad (3.63)$$

where  $(l, p)$  corresponds to the corner pixel on the SLM.

Because of the requirement that  $\xi_x = 0$  and  $\xi_y = 0$ , there will only be one pixel grating from each page that contributes to the reconstructed field for the page and pixel under consideration. We can simplify the notation, by implicitly assuming all the other necessary indices and vector computations, only leaving the page index:

$$E \propto \sum_m a_m \eta_m e^{i\phi_m} \quad (3.64)$$

By separating out page  $M_r$  from the sum, we can write the output field as the desired data embedded in an additive field noise:

$$E \propto a_{M_r} + \sum_{m \neq M_r} a_m \eta_m e^{i\phi_m} \quad (3.65)$$

$$= a_{M_r} + E_n \quad (3.66)$$

Because the data bits are random, the field noise is likewise random. The first and second moments will strongly define how easy or difficult it is to distinguish the case of  $a_{M_r} = 1$  from  $a_{M_r} = 0$ . We characterize this by defining the noise-to-signal ratio as:

$$\text{NSR} \triangleq \frac{\sqrt{\sigma_1^2 + \sigma_0^2}}{\mu_1 - \mu_0} \quad (3.67)$$

where  $\mu_j$  and  $\sigma_j^2$  are the first and second moments of the detected pixel irradiance.  $j$  refers to the stored 0 or 1 pixel value.

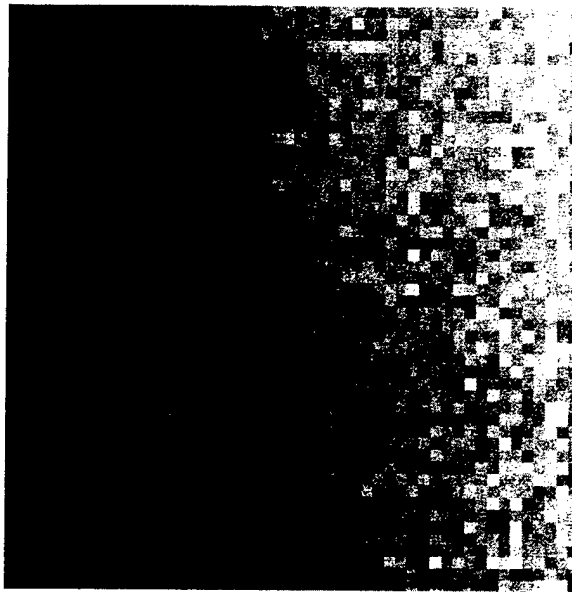


Figure 3.9: NSR in upper right quadrant of  $m = M_r$  page.

The pixel irradiance is proportional to the square of the electric field:

$$I \propto |E|^2 \quad (3.68)$$

$$= a_{M_r} + |E_n|^2 + 2a_{M_r} \text{Re}[E_n] \quad (3.69)$$

Fig. 3.9 shows a simulation of the NSR with respect to every pixel in the upper right quadrant of the  $m = M_r$  page. Notice that columns have the same NSR value as we expect due to the degeneracy in the  $\hat{y}$  direction.

### 3.5.1 Apodizer Shapes

We considered a variety of apodized reference beam shapes in order to characterize the effect of many parameters relevant to apodization, such as sidelobe suppression, main lobe width, and sidelobe decay rate.

In this study we only consider amplitude apodization functions. Phase apodization is a possible alternative technique which we did not investigate. Table 3.1 lists the considered apodizer shapes which are described by their normalized amplitude transmittance function,  $t(z)$ , defined over the interval  $[-\frac{1}{2}, +\frac{1}{2}]$ . Note that some of the apodizers are parameterized by  $\beta \in [0, 1]$ .

Figs. 3.10-3.11 plot the transmittance function and spectrum for the apodizers considered. The spectrum is shown as the log-magnitude in dB. Notice that the peak value of the spectrum represents the lost power when using an absorptive apodizers to construct the apodized electric field profile.

Apodizer Type	$t(z)$
Rectangle	1
Trapezoid	$\begin{cases} 1 - 2 z /\beta &  z  \geq \frac{1}{2}(1 - \beta) \\ 1 & \text{else} \end{cases}$
Triangle	$1 - 2 z $
Hamming	$0.5435 + 0.4565 \cos 2\pi z$
Gaussian	$e^{-\frac{1}{2}(2\beta z)^2}$
Raised Cosine	$\cos^\beta \pi z$
Tukey	$\begin{cases} 1 + \cos \left[ \frac{\pi(2 z  - \beta)}{1 - \beta} \right] &  z  \geq \beta/2 \\ 1 & \text{else} \end{cases}$

Table 3.1: Apodizer functions

### 3.5.2 NSR results

The noise statistics on the irradiance random variable will determine when cross talk noise limits the storage of additional pages. Consider the NSR when the Bragg selectivity function is determined by the absorption corrupted modulation depth. In fig. 3.12 we plot the NSR as a function of the number of pages in



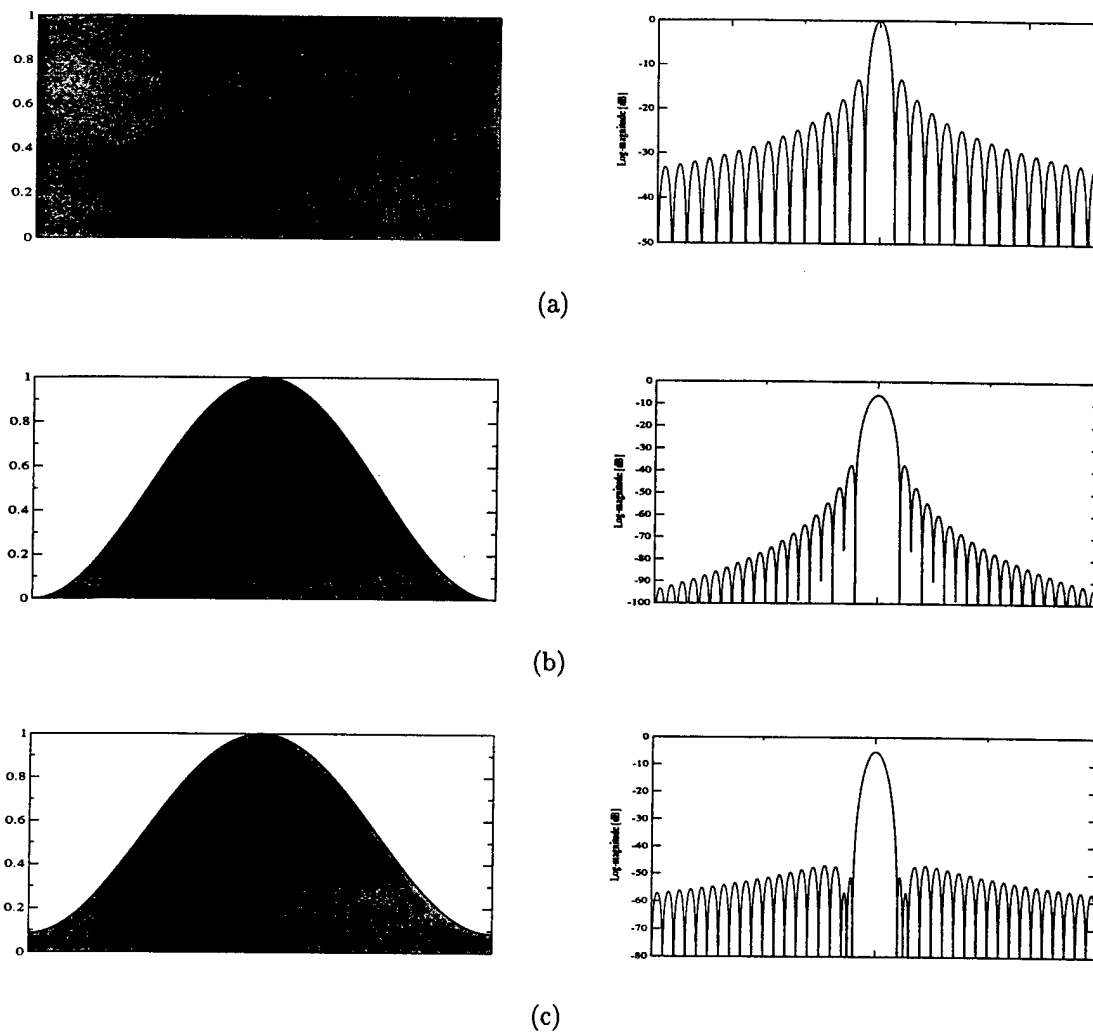


Figure 3.10: Apodizer transmittance and spectrum of (a) rectangle, (b) hamming, (c) raised cosine.

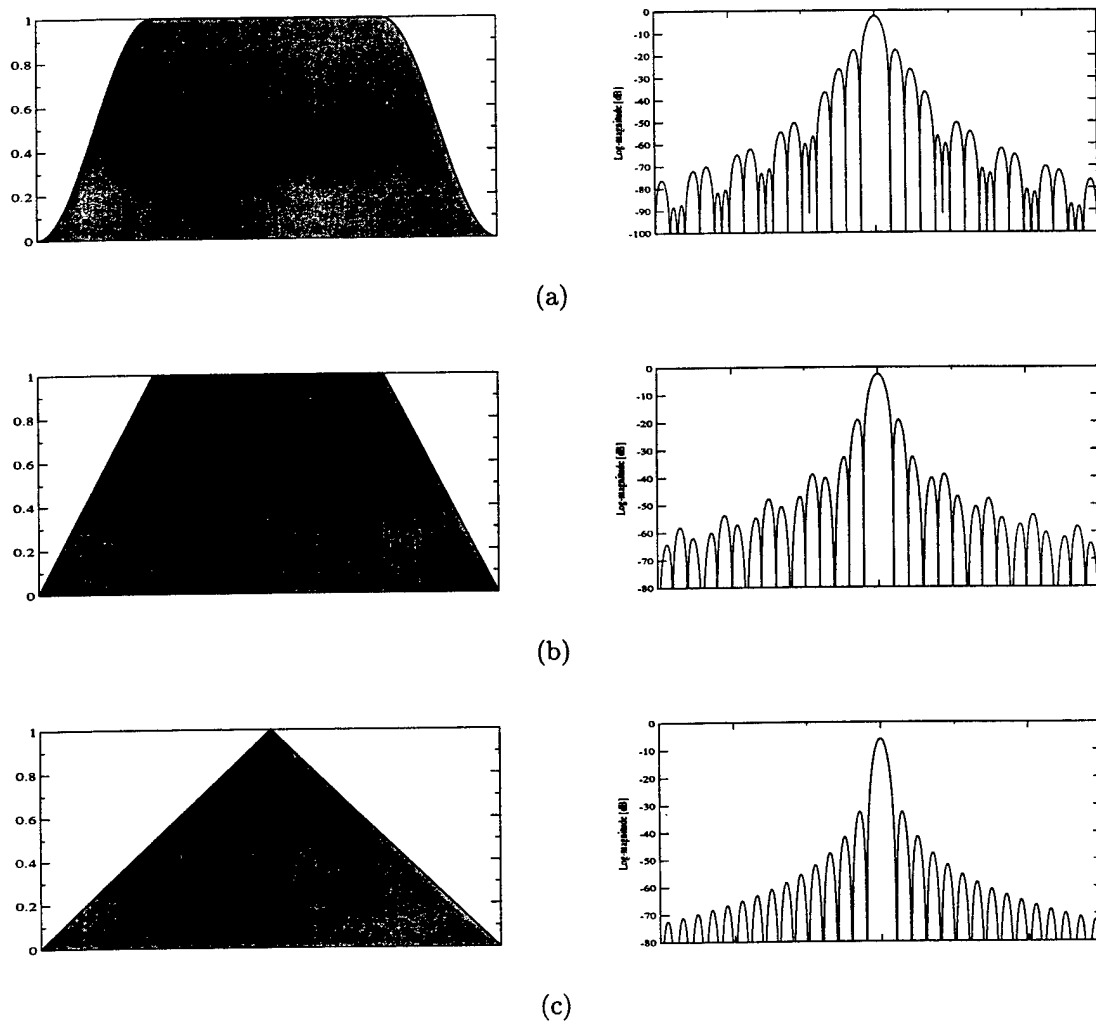


Figure 3.11: Apodizer transmittance and spectrum of (a) tukey, (b) trapezoid, (c) triangle.

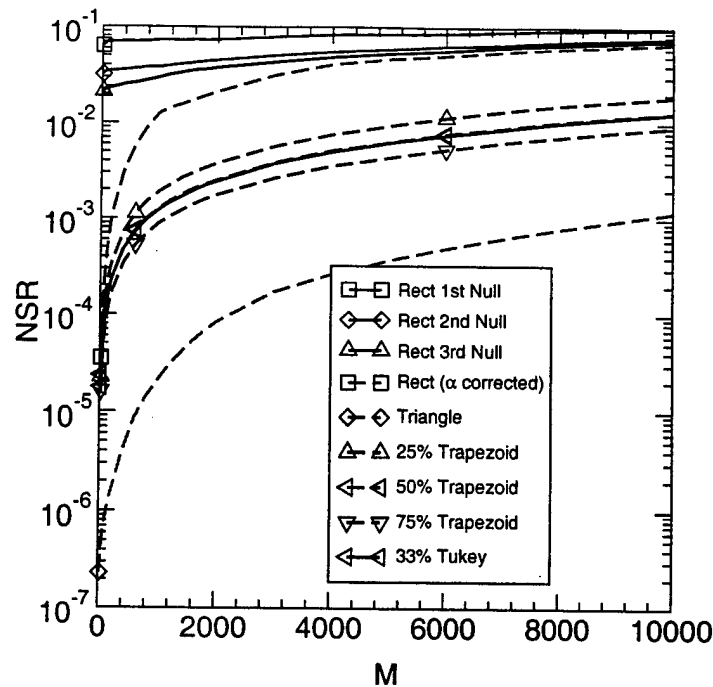


Figure 3.12: NSR (random page phase) for 1 cm crystal with  $\alpha = 0.55 \text{ cm}^{-1}$ .

memory,  $M$  for a variety of apodizers in addition to first null, second null, and third null sinc storage. Note that all the non-rectangular apodizers are implicitly absorption-corrected. We see from the default first, second, and third null storage that the NSR can be reduced by decreasing the multiplexing density. But clearly, if the NSR must be lowered, it is far more powerful to correct the absorption and use first null storage, or use one of the other windowing functions, such as the 50% trapezoidal apodizer.

When the pages add coherently (fig. 3.13), we see the NSR grows much faster than with the random phase. This result is expected as the random phase term serves to average out much of the cross talk contributions.

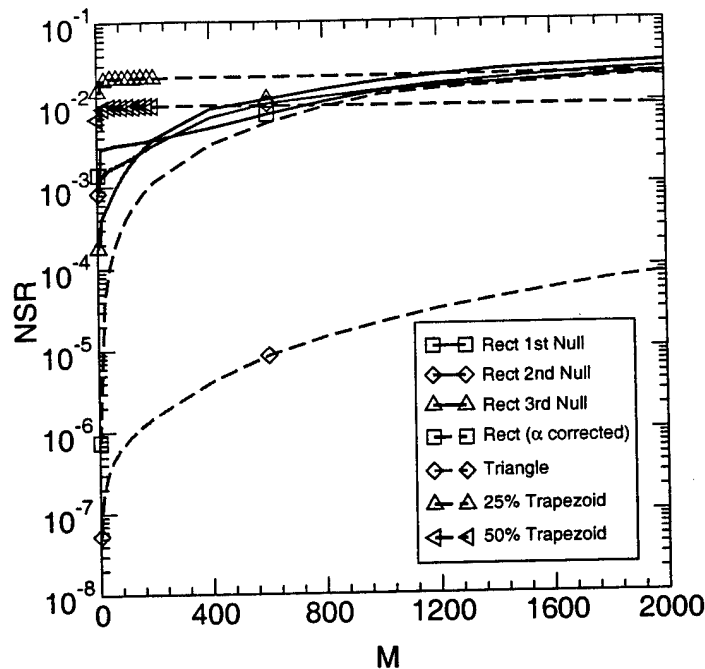


Figure 3.13: NSR (coherent phase) for 1 cm crystal with  $\alpha = 0.55 \text{ cm}^{-1}$ .

When there is an angular pointing error associated with achieving the recording and reconstruction angles, then the cross talk from neighboring holograms establishes a large noise floor. Fig. 3.14 shows the histogram from an experiment using a New Focus picomotor to repeatably point at the same angle after random movements away from the desired angle. The standard deviation of the pointing accuracy was measured to be  $7.6 \mu\text{rad}$ . This corresponds to 3.3% of a Bragg null for a 0.5 cm crystal. The irradiance diffraction efficiency is plotted and labeled on the right axis. The histogram count is labeled on the left axis.

The jitter dominated IPI is shown in fig. 3.15 where the pointing error is zero mean and bounded below  $\pm 3.3\%$  of the null spacing. We see in this case, the

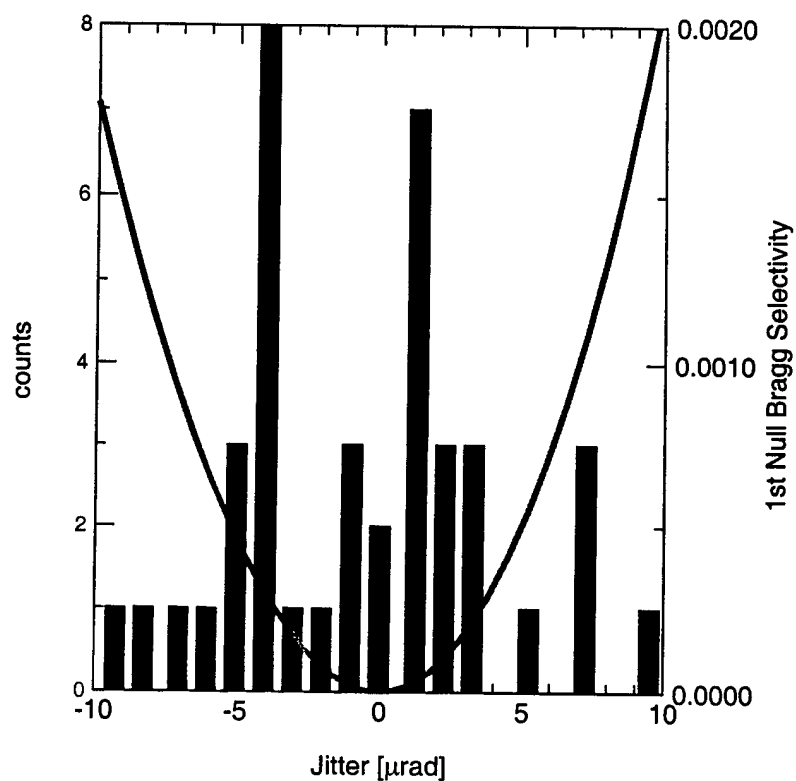


Figure 3.14: Experimental jitter histogram from repeated measurements on pointing accuracy and repeatability of New Focus picomotor. The standard deviation is  $7.6 \mu\text{rad}$ , which corresponds to 3.3% of a Bragg null spacing for a 0.5 cm crystal. The quadratic curve and the right axis refer to the Bragg selectivity function centered at the first null.

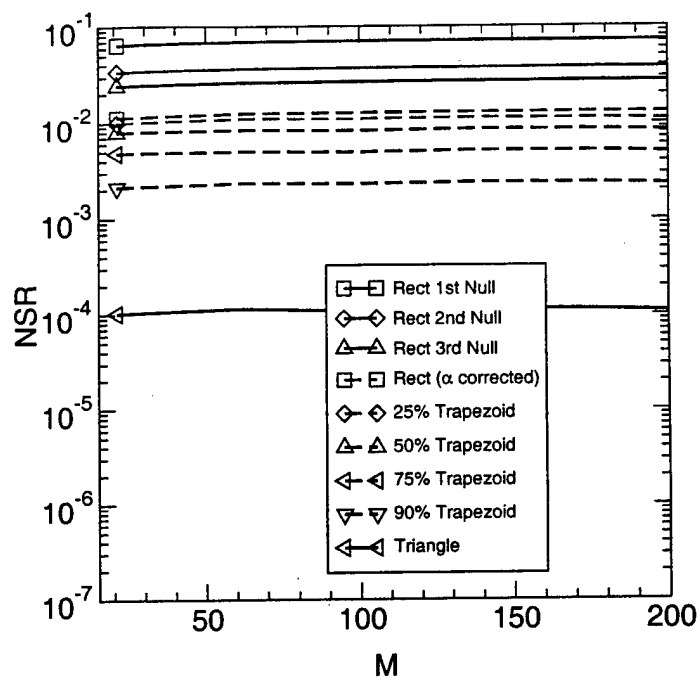


Figure 3.15: Jitter dominated IPI noise;  $L = 0.45$  cm,  $\alpha = 0.55$  cm $^{-1}$ , 3.3% angular jitter.

cross talk does not scale significantly with  $M$  as the noise is saturated by the relative diffraction efficiency of the neighboring holograms.

### 3.6 Apodized $M/\#$

In this section we consider the impact of absorption on the recording and erasure dynamics of photorefractive volume holograms.  $\alpha$  is a key component in the photorefractive effect driving the time rate of grating formation and erasure. When the absorption is very small, holographic gratings record slowly and erase slowly. When the absorption is larger, gratings record faster but subsequently erase faster. Somewhere between the two extreme cases exists an optimal absorption coefficient for a given set of material and system parameters. This relation

was derived from the underlying crystal physics and material parameters in reference [42]. The absorption is optimal in the sense that it maximizes the system metric  $M/\#$ .<sup>31</sup>  $M/\#$  provides the scaling constant relating the Bragg-matched page diffraction efficiency and the number of multiplexed pages  $M$ :

$$|\eta(\xi_z = 0)|^2 = \left( \frac{M/\#}{M} \right)^2, \quad (3.70)$$

where  $\eta(\xi_z = 0)$  is the Bragg-matched amplitude diffraction efficiency considered in section 3.3. Following a similar approach to reference [42] we develop the  $M/\#$  for the apodized system using Fe:LiNbO<sub>3</sub> as the photorefractive medium.

The reconstruction reference beam (eq. 3.23) incident on the crystal has a total power,  $P_{in}$ , of:

$$P_{in} \triangleq \int_0^H \int_0^L |R_0 R(z)|^2 dy dz \quad (3.71)$$

$$= H R_0^2 \int_0^L |R(z)|^2 dz \quad (3.72)$$

$$= H R_0^2 P_R \quad (3.73)$$

where for convenience we define the power in the apodizer shape as:

$$P_R \triangleq \int_0^L |R(z)|^2 dz \quad (3.74)$$

The diffracted power,  $P_{out}$ , can be found by integrating over the angular spectrum of the diffracted wavevectors:

$$P_{out} = \iint \left| A(\vec{k}_d, \vec{k}_i) \text{sinc}(k_{d,x} W) \text{sinc}(k_{d,y} H) \right|^2 dk_{d,x} dk_{d,y} \quad (3.75)$$

which by Parseval's theorem<sup>27</sup> can be reexpressed as the power in the reciprocal domain:

$$P_{out} = \int_0^H \int_0^W \left| \frac{E_d(0)}{WH} \text{rect}\left(\frac{x}{W}\right) \text{rect}\left(\frac{y}{H}\right) \right|^2 dx dy \quad (3.76)$$

$$= \frac{|E_d(0)|^2}{WH} \quad (3.77)$$

where  $E_d(\xi_z)$  was defined in eq. 3.28.

The amplitude diffraction efficiency is the ratio of the square root of the input and diffracted powers, allows us to represent the Bragg-matched diffraction efficiency (BSF at  $\xi_z = 0$ ) as:

$$\eta(0) = \sqrt{\frac{P_{out}}{P_{in}}} \quad (3.78)$$

$$= \frac{|E_d(0)|}{HR_0\sqrt{WP_R}} \quad (3.79)$$

$$= \frac{\epsilon_0 n_0^4 r_{13}}{H\sqrt{WP_R}} \left| \iiint E_1(\vec{r}) R(z) S_\alpha(x, z) e^{-i\vec{K}_g \cdot \vec{r}} d\vec{r} \right| \quad (3.80)$$

For small recording exposures the space charge field and the modulation depth are related as:

$$|E_1(\vec{r}; t)| \propto m(x, z) E_{sc}(\alpha) (1 - e^{-t/\tau_l(x, z)} e^{-i\omega_l(x, z)t}) \quad (3.81)$$

where the new parameters are defined in Burr's thesis [42].  $\tau_l$  is the local recording time constant.  $\omega_l$  is the imaginary component of the local recording time constant.  $E_{sc}$  summarizes a number of material properties. It can be thought of as a material scaling parameter. It is important to note that it depends on  $\alpha$  among other things.



In terms of the saturation amplitude and recording time constant, the space charge field evolves according to:

$$|E_1(\vec{r}; t)| = A_0 [1 - e^{-t/\tau_r}] \quad (3.82)$$

Taking the time derivative at  $t = 0$  for both forms allows us to express the recording slope ( $A_0/\tau_r$ ) as:

$$A_0/\tau_r = \frac{\epsilon_0 n_0^4 r_{13}}{\tau_x H \sqrt{W P_R}} |E_{sc}(\alpha) (1 + i\tau_l \omega_l)| \cdot \left| \int \int \int S_0 W_0 W(z) R(z) e^{-\frac{\alpha}{2}(x+L)} d\vec{r} \right| \quad (3.83)$$

$$= \frac{\epsilon_0 n_0^4 r_{13} S_0 W_0 e^{-\frac{\alpha}{2}L} (1 - e^{-\alpha W})}{\tau_x \sqrt{W P_R}} |E_{sc}(\alpha) (1 + i\tau_l \omega_l)| \cdot \left| \int_0^L W(z) R(z) dz \right| \quad (3.84)$$

During erasure, the space charge field decays as  $e^{-t/\tau_e}$ .  $\tau_e$  can be found by taking the ratio of  $\eta$  and the derivative at  $t = 0$ :

$$\tau_e = \frac{\tau_x \int_0^L R(z) W(z) dz}{S_0^2 \int_0^L R(z) W(z) e^{-\alpha z} dz + W_0^2 \frac{1+e^{-\alpha W}}{2} \int_0^L R(z) W(z) |W(z)|^2 dz} \quad (3.85)$$

Finally, the  $M/\#$  can be computed as the product of the recording slope and the erasure time constant:

$$M/\# \triangleq (A_0/\tau_r) \tau_e \quad (3.86)$$

$$= \frac{1}{2} k_0 n_0^3 r_{13} |E_{sc}(\alpha)| \left( \frac{1 - e^{-\alpha W}}{\alpha} \right) \frac{S_0}{W_0} \sqrt{\frac{L}{W}} \frac{e^{-\alpha L/2}}{\sqrt{P_R}} \times \frac{\left( \int_0^L R(z) W(z) dz \right)^2}{\left( \frac{S_0}{W_0} \right)^2 \int_0^L R(z) W(z) e^{-\alpha z} dz + \frac{1 + e^{-\alpha W}}{2} \int_0^L R(z) W(z) |W(z)|^2 dz} \quad (3.87)$$

where  $k_0 = 2\pi/\lambda_0$ ,  $n_o$  is the ordinary index of refraction,  $r_{13}$  is electro-optic coefficient, and  $E_{sc}(\alpha)$  is the space-charge field amplitude which depends on a number of crystal parameters including  $\alpha$ .

In figure 3.16 we plot the  $M/\#$  for the three apodization cases versus the absorption coefficient. For each choice of  $\alpha$  the beam ratio is selected to maximize the  $M/\#$ . Recording apodization restores the ideal Bragg nulls but suffers a 6.8% loss in  $M/\#$ . Apodization of the reconstruction beam loses 1.5% in  $M/\#$  and nearly perfectly restores the ideal nulls.

An important result to notice is that the optimum absorption coefficient (that maximizes  $M/\#$ ) has shifted due to apodization. For a  $1 \times 1 \times 1 \text{ cm}^3$  LiNbO<sub>3</sub> crystal, the optimal  $\alpha$  is 0.727, 0.697, 0.608  $\text{cm}^{-1}$  for no apodization, reconstruction beam apodization, and recording beam apodization, respectively.

### 3.7 Summary

In this chapter we have presented some theoretical results about page-to-page cross talk in photorefractive media. We saw the the Bragg selectivity function can be related to the transverse electric profile through a Fourier transform. This allows modification of the reference beam to reduce cross talk and correct for deleterious material effects such as absorption. In addition, we developed the modifications necessary to describe the  $M/\#$  of an apodized system. Simulations showed that there was only a minor cost in reduction of  $M/\#$  when using apodization to correct the influence of absorption and restore the ideal Bragg nulls.

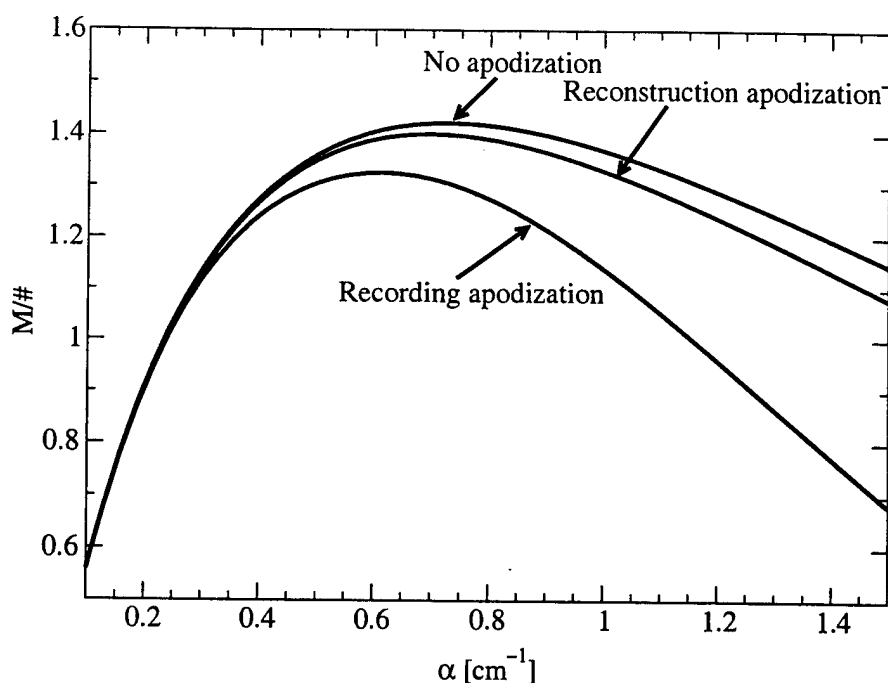


Figure 3.16:  $M/\#$  versus absorption in a  $1 \times 1 \times 1 \text{ cm}^3$  Fe:LiNbO<sub>3</sub> crystal for no apodization, reconstruction beam apodization, and recording beam apodization.

**Notes** Portions of this work have been published in *Proceedings-of-the-SPIE* as described in reference [47]. The basic derivation of  $M/\#$  is due to Geoff Burr.<sup>42</sup> Extensions to incorporate apodization in the derivation were originally considered by a former OCPL group member, Xue-Wen Chen. There are only a few minor differences between his and my derivation.